Article

Cell Reports

Elongation-Competent Pauses Govern the Fidelity of a Viral RNA-Dependent RNA Polymerase

Graphical Abstract

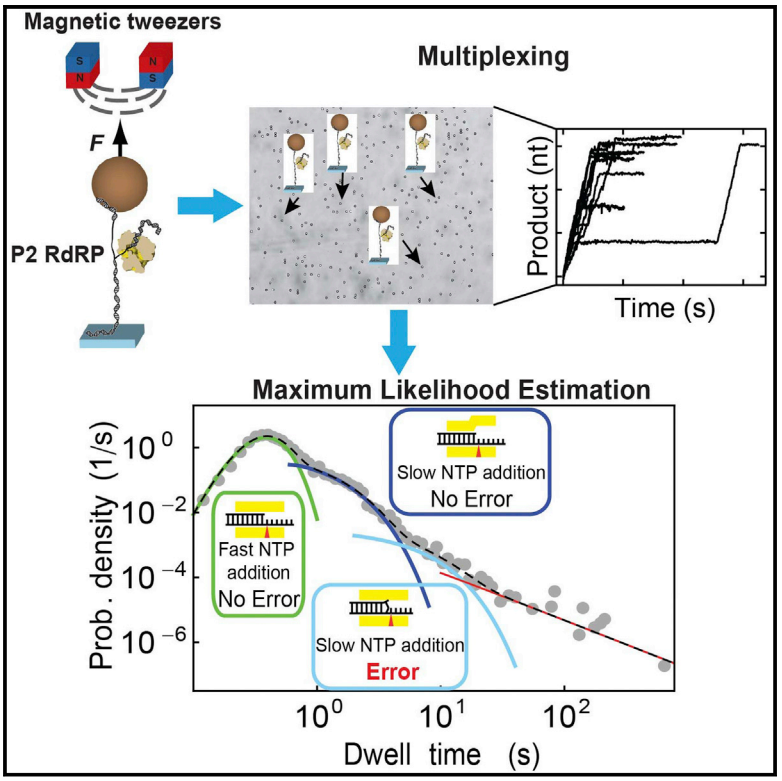

Authors

David Dulin, Igor D. Vilfan, ...,
Martin Depken, Nynke H. Dekker

Correspondence

minna.poranen@helsinki.fi (M.M.P.),
s.m.depken@tudelft.nl (M.D.),
n.h.dekker@tudelft.nl (N.H.D.)

In Brief

Using high-throughput single-molecule magnetic tweezers, Dulin et al. show that viral RdRP elongation is highly dynamic. Applying an unbiased analysis based on maximum likelihood estimation, they demonstrate that short pauses are the signature of an unknown error-prone nucleotide incorporation pathway.

Highlights

- The RNAP elongation dynamic of dsRNA virus is captured by magnetic tweezers
- Large sets of high-resolution data allow quantification of polymerase fidelity
- Maximum likelihood estimation allows extraction of critical model parameters
- Errors are predominantly incorporated via new error-prone catalytic pathway

Dulin et al., 2015, Cell Reports *10*, 983–992
February 17, 2015
http://dx.doi.org/10.1016/j.celrep.2015.01.031

Cell Reports
Article

Elongation-Competent Pauses Govern the Fidelity of a Viral RNA-Dependent RNA Polymerase

David Dulin,[1,4] Igor D. Vilfan,[1,5] Bojk A. Berghuis,[1] Susanne Hage,[1] Dennis H. Bamford,[2,3] Minna M. Poranen,[2,*] Martin Depken,[1,*] and Nynke H. Dekker[1,*]
[1]Department of Bionanoscience, Kavli Institute of Nanoscience Delft, Delft University of Technology, Lorentzweg 1, 2628 CJ Delft, the Netherlands
[2]Department of Biosciences
[3]Institute of Biotechnology
University of Helsinki, Viikki Biocenter 2, P.O. Box 56 (Viikinkaari 5), 00014 Helsinki, Finland
[4]Present address: Biological Physics Research Group, Department of Physics, Clarendon Laboratory, University of Oxford, Parks Road, Oxford OX1 3PU, UK
[5]Present address: Pacific Biosciences, 1380 Willow Road, Menlo Park, CA 94025, USA
*Correspondence: minna.poranen@helsinki.fi (M.M.P.), s.m.depken@tudelft.nl (M.D.), n.h.dekker@tudelft.nl (N.H.D.)
http://dx.doi.org/10.1016/j.celrep.2015.01.031

SUMMARY

RNA viruses have specific mutation rates that balance the conflicting needs of an evolutionary response to host antiviral defenses and avoidance of the error catastrophe. While most mutations are known to originate in replication errors, difficulties of capturing the underlying dynamics have left the mechanochemical basis of viral mutagenesis unresolved. Here, we use multiplexed magnetic tweezers to investigate error incorporation by the bacteriophage Φ6 RNA-dependent RNA polymerase. We extract large datasets fingerprinting real-time polymerase dynamics over four magnitudes in time, in the presence of nucleotide analogs, and under varying NTP and divalent cation concentrations and fork stability. Quantitative analysis reveals a new pause state that modulates polymerase fidelity and so ties viral polymerase pausing to the biological function of optimizing virulence. Adjusting the frequency of such pauses offers a target for therapeutics and may also reflect an evolutionary strategy for virus populations to track the gradual evolution of their hosts.

INTRODUCTION

RNA viruses are responsible for many human pandemics, including hepatitis C, polio, influenza, and dengue fever. Because of their high mutation rates, RNA viruses evolve rapidly and are difficult to target with vaccines (Lauring et al., 2013). On the molecular level, the dominant source of mutations is the error-prone RNA-dependent RNA polymerases (RdRPs) responsible for replicating the viral genomes (Vignuzzi et al., 2006). A high mutation rate increases evolvability, but also induces many deleterious mutations, and a delicate balance needs to be struck to ensure the pathogenicity of the viral population. Given the strict demands on the precision of mutation rates, RdRPs have become an important target for antiviral therapies that seek to either decrease (Crotty et al., 2000; Vignuzzi et al., 2005) or increase (Vignuzzi et al., 2008) RdRP replication fidelity. Understanding how RdRPs influence viral mutation rates therefore carries direct implications for human health and the development of antiviral therapies, but is also of fundamental importance for our comprehension of viral evolution. Despite this, little is known about the dynamics of RNA elongation by RdRPs (Yang et al., 2012) and in particular of the nucleotide selection process—the origin of most mutations.

Direct probing of error incorporation is challenging, as errors are infrequent random events easily masked in bulk measurements. Stop-flow and quench-flow experiments have greatly elucidated the dynamics of nucleotide addition, but such experiments often rely on nucleotide starvation conditions to induce otherwise rare error-incorporation events (Jin et al., 2011, 2012; Johnson, 2008; Yang et al., 2012); as the polymerization dynamics is severely perturbed under such conditions, it is not a priori evident that the error probabilities estimated in this way represent error rates under physiological conditions. Single-molecule experiments (Dulin et al., 2013; Geertsema and van Oijen, 2013; Larson et al., 2011) do in principle have the potential to detect error incorporation in the presence of all nucleotides, but the limited throughput of these experiments has so far precluded a detailed statistical study of such rare events.

To gain a deeper insight into the origin of viral mutagenesis, we here study error incorporation of a model RdRP at the single-molecule level. Specifically, as all the structurally characterized RNA-dependent viral polymerases share a high degree of structural conservation (Mönttinen et al., 2014; Ng et al., 2008), we use the well characterized P2 (Figure 1A)—the RdRP of the double-stranded RNA (dsRNA) bacteriophage Φ6—as a model system for viral RdRPs and RTs (Butcher et al., 2001; Makeyev and Grimes, 2004). To overcome limitations induced by bulk averaging and limited statistics, we

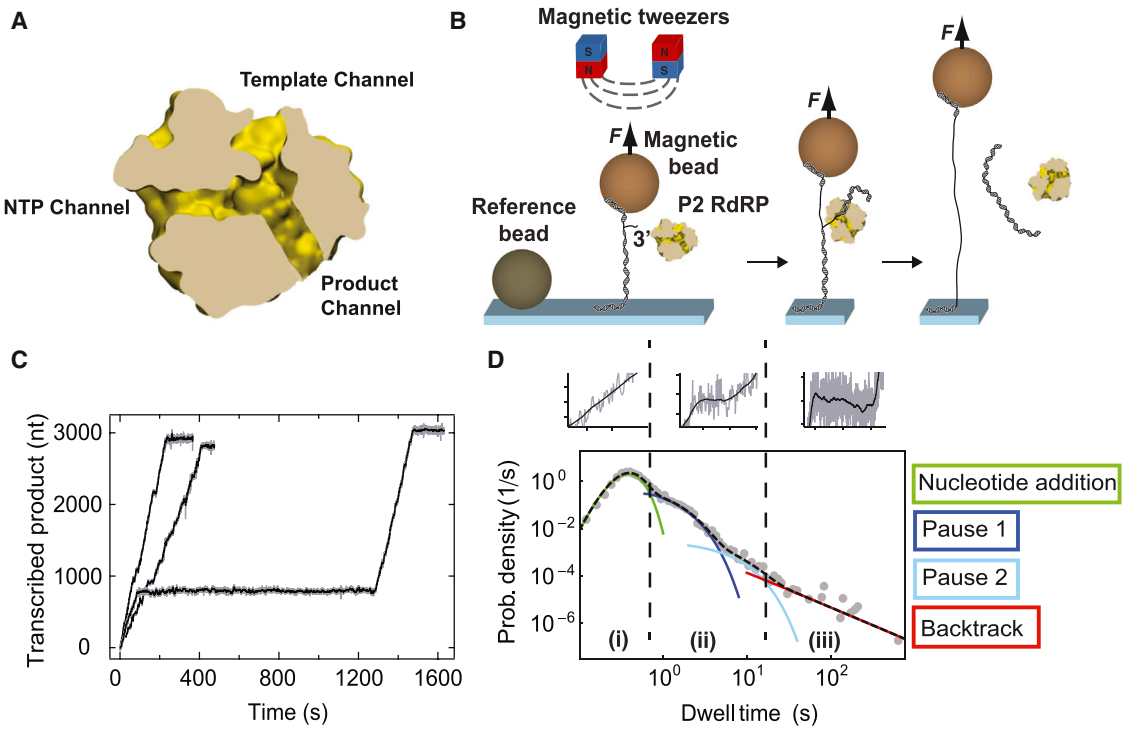

Figure 1. Detecting P2 Activity at the Single-Molecule Level

(A) Illustration of a cross-section of P2 in elongation, displaying the NTP and template tunnels (according to structure of the initiation complex, PDB number: 1UVI; Salgado et al., 2004) together with the product channel, which has been drawn in manually for purposes of illustration.

(B) Schematic of the experimental setup for monitoring P2 transcription on magnetic tweezers. In all three panels, *F* refers to the force applied by the magnetic tweezers. A primarily duplex RNA is tethered to a magnetic bead at one extremity and to a surface at the other. This RNA construct is built on a 4.2-kb plus strand to which a 2.8-kb template strand for P2 transcription is hybridized. The template strand is fully complementary to the 4.2-kb plus-strand apart from a 15-nt overhang at the 3′ end to facilitate enzyme initiation (Figure S1).

(C) Three typical traces of P2-catalyzed transcription representing the increase in product length versus time at 20 pN force and $[NTP]_{opt}$. All three traces were acquired at 25 Hz (gray) and low-pass filtered at 0.5 Hz (black). These three traces present different dynamic behavior that is attributable to three unique P2 enzymes. The leftmost trace includes almost no pauses. The middle trace is interrupted by few short pauses, and the rightmost trace includes two distinct regions of fast transcription activity separated by a very long pause.

(D) The dwell-time distribution is extracted from 52 traces of P2 transcription activity acquired at 20 pN and $[NTP]_{opt}$ (gray dots). We fit this distribution to a stochastic-pausing model (Supplemental Information) by using MLE (dashed black line). For clarity, we individually plot each contribution to the dwell-time distribution: in green, the Gamma distribution; in dark blue, the first short pause (Pause 1); in cyan, the second short pause (Pause 2); and in red, the power law distribution of pause times originating in backtracking. On top of the histogram are plotted representative events in P2 activity: from left to right (1) fast incorporation without pause, described by the Gamma distribution; (2) short pauses, described by the two exponential distribution; and (3) long backtracked pauses, described by a power law distribution. The distinct appearance of the nucleotide-addition peak and the fact that the fitted Gamma distribution captures both its width and average (using a single free parameter, assuming that the polymerase takes 1-nt steps) show that our approach is not appreciably affected by experimental noise and avoids convolving elongation with pausing (Supplemental Information; Figure S3A).

have developed a stable and massively *multiplexed* magnetic-tweezers assay (Figure S1B) that retains the single-molecule resolution while producing the statistics necessary to study rare error-incorporation events. We collected ~1,000 elongation traces (RdRP position versus time over a maximum of 2,800 nucleotides [nt]) at varying nucleotide (NTP) and divalent cation concentrations in the presence of nucleotide analog and under varying fork stability (Figures 1B and S1E). Our elongation traces are highly stochastic (Figure 1C), with force-insensitive and rapid elongation (~20 nt/s) interrupted by pauses of duration 1–10 s and a small population of pauses lasting 10–1,000 s. Based on a maximum-likelihood analysis tailored to our large single-molecule force-spectroscopy data sets, we uncover evidence that the ϕ6 RdRP, and by extension other RdRPs and RTs, utilizes two distinct but coupled pathways for error incorporation: one high-fidelity pathway without significant pausing and one low-fidelity pathway accessible through a novel pause state. Direct mutations of the active site that have a large effect on mutation rates are generally deleterious (Acevedo et al., 2014). Therefore, the ability to gradually tune between two pathways with different inherent fidelities offers an attractive alternative evolutionary strategy to achieve the precise mutation rates needed to track the evolution of the host and ensure continued viral pathogenicity. Detailed information regarding how error probabilities are dynamically set could also facilitate the development and refinement of drug therapies specifically targeting viral mutagenesis (Crotty et al., 2000; Vignuzzi et al., 2005, 2008).

RESULTS

Multiplexed Magnetic Tweezers Detail RdRP Dynamics on Subsecond to Hour Timescales

In our magnetic tweezers assay, dozens of magnetic beads (Figure S1B) are tethered to a surface via dsRNA (Figure 1B). When P2 is added to the reaction buffer, it initiates at a 3′ overhang present on each tether (Figures 1B and S1A) (Butcher et al., 2001; Makeyev and Bamford, 2000a; Sarin et al., 2009; Wright et al., 2012). By processively elongating the RNA product, P2 converts the tethered dsRNA into single-stranded RNA (ssRNA) while producing a free dsRNA strand (Figure 1B). Because of the length difference between ssRNA and dsRNA (Figure S1C), the motion of each elongating P2 molecule can be determined from the change in vertical position of the magnetic bead (Figure 1B) with an experimental spatial resolution of ~5 nt or better, depending on the applied force and the length of the exposed ssRNA (with the instrumental noise, measured to equal 0.3 nm at 0.5 Hz on a fixed bead, providing the ultimate limit; Figure S1B). The absolute bead position at initiation is determined with a 10- to 20-nt precision, limited by occurrences of P2 pausing shortly after initiation. Each trace originates in the activity of a single P2, as the initiation site is removed once P2 has converted the 3′ overhang into duplex RNA (Figure 1B). Different traces taken during the same experiment differ remarkably (Figures 1C and S1D) and demonstrate the highly stochastic nature of P2 elongation dynamics; for example, in Figure 1C, the fastest enzyme shown spent at most a few seconds in a paused state, while the slowest enzyme paused for more than 1,000 s.

Maximum-Likelihood Estimation Based on the General Sequence Independent Elongation Model with Two Pauses and Backtracks

To analyze the stochastic P2 elongation dynamics, we perform a probabilistic analysis of the times it takes the polymerase to transcribe through consecutive windows of 10 nt along the trace. This window size is set to equal at least twice the experimental spatial resolution of the noisiest configuration (lowest force, ssRNA tethers) in order to avoid noise-triggered crossings in and out of the dwell-time window. The recorded times are referred to as dwell times. By collecting a large number of dwell times (for the exact total number of dwell time in each condition presented here, see Figure S1E), we can construct empirical dwell-time distributions (Figure 1D) that capture the probabilistic nature of P2 dynamics with high precision (see typical error bars indicated in Figure S2C). A few characteristic features become immediately apparent (Figure 1D; Supplemental Information): (1) a short-time peak—the nucleotide-addition peak—originating from P2 elongating through the dwell-time window without pausing, with the position of the apex of this peak reflecting the typical time taken to cross the dwell-time window without pausing, and its width is set by the number of steps taken in doing so; (2) a shoulder situated at intermediate times, corresponding to one or more short pauses with exponentially distributed lifetimes; and (3) a long-lived pause with a broad distribution of lifetimes that is consistent with a polymerase paused by backtracking (Cheung and Cramer, 2011; Depken et al., 2009; Galburt et al., 2007; Shaevitz et al., 2003; Voliotis et al., 2008). As described in the Supplemental Information, we use the Bayes-Schwartz information criterion (Schwarz, 1978) to objectively determine that the data support the existence of two separate short pauses—Pauses 1 and 2—represented in the shoulder (2) of our measured dwell-time distributions (Figure 1D). We use maximum-likelihood estimation (MLE) (Supplemental Information) to fit a general stochastic-pausing model to each measured dwell-time distribution and extract the nucleotide addition rate (k_{na}), the probability of nucleotide addition without pausing (P_{na}), as well as the pause entrance probabilities (P_1 and P_2) and the exit rates (k_1 and k_2) for the two short pauses. The fitting parameters extracted from the MLE are not altered by the noise encountered in our experiments (Figure S3A). As the exponential-pause shoulders in the dwell-time distributions hide the features needed to determine the amount of backtracking, we merely include this pause type to avoid introducing a late-time cutoff that might bias the analysis. Under any single realization of experimental conditions, the fitted dwell-time distribution is consistent with a multitude of reaction schemes including the specified pauses. In the Discussion, we argue that the data from our concentration sweeps suggest a particular minimal reaction scheme. As we cannot accurately determine the absolute position of the RdRP, we do not include sequence effects in our model. In the Supplemental Information, we also argue why sequence effects are not likely to be significant. Even so, if there is strong sequence dependence, our parameter estimates can be seen as representing averages over sequence.

The NTP Concentration Dependence of P2 Catalyzed RNA Elongation Dynamics

To probe the dynamics of nucleotide incorporation, we next vary the nucleotide concentration in our assay in the μM to mM range, all at a constant force (30 pN) and nucleotide stoichiometry (Figures 2 and S2A). We find that the average time P2 required to transcribe the template increases with a decrease in the NTP concentration: from 130 s at the highest concentration $[NTP]_{opt}$ (a mM concentration optimized for P2 initiation; see Supplemental Information and Makeyev and Bamford, 2000b; Vilfan et al., 2008) to 1,750 s at $[NTP]_{opt}/500$. Comparing the dwell-time distributions obtained at $[NTP]_{opt}$ and $[NTP]_{opt}/100$ (Figure 2A, black circles and red triangles, respectively), we see that a hundred-fold decrease in the nucleotide concentration only results in a slight shift in the nucleotide-addition rate (as judged from the position of the apex of the nucleotide-addition peak in Figure 2A). At the same time, the time spent in short pauses is greatly increased (as judged from the weight under the exponential shoulders in Figure 2A). These results suggest that in the concentration range examined, the major shift in dynamics originates in a change of pausing behavior, and not in a slowdown of the nucleotide-addition process. The empirical dwell-time distribution is well described by our stochastic-pausing model over the concentration range examined (Figures 2B and 2C). Importantly, since we can directly judge from Figure S2A if the elongation peak is discernable against the background of the pausing shoulder, we can determine the concentration range over which it is possible to estimate the bare nucleotide addition rate without the risk of inadvertently including the effect of pauses. This constitutes a clear advantage

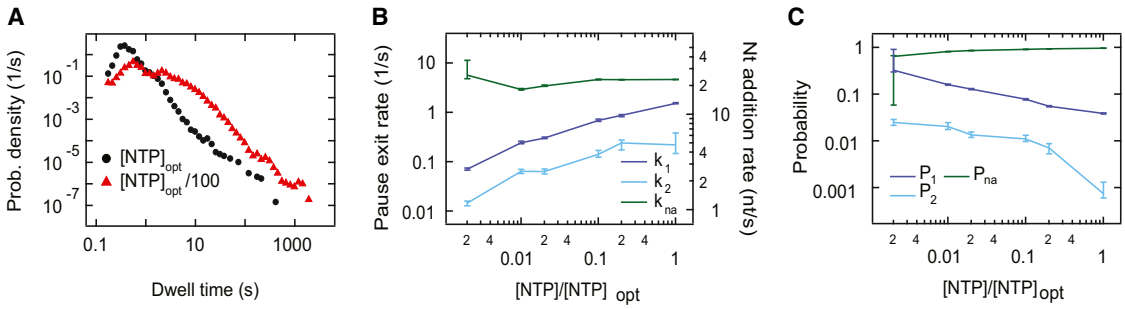

Figure 2. The Nucleotide Concentration Dependence of P2 Transcription Dynamics

(A) The empirical dwell-time distributions for two different NTP concentrations at the same force (30 pN): black dots, $[NTP]_{opt}$; red triangles, $[NTP]_{opt}/100$.

(B) The pause exit and nucleotide addition rates as a function of NTP concentration. The error bars represent the SD of a MLE procedure applied to 200 bootstrapped data sets. The nucleotide addition rate (right axis) is represented by green dots connected by green lines as guides for the eye. The value of the nucleotide addition rate at $[NTP]_{opt}/500$ is not well estimated because of the disappearance of the Gamma distribution behind Pause 1 distribution (Figure S2A). The pause exit rates (left axis) are represented by dots connected by lines as guides for the eye (dark blue, k_1; cyan, k_2).

(C) Probability for P2 to be in one of the three different states (green, nucleotide addition; dark blue, Pause 1; cyan, Pause 2) as a function of relative NTP concentration.

over standard attempts of fitting out pause-free velocities as detailed in the Supplemental Information and in Figures S3B and S3C.

Error Incorporation Is Associated with P2 Pausing

To probe how error incorporations affect RdRP dynamics, we introduced the nucleotide analog inosine 5′-triphosphate (ITP) to the reaction buffer. ITP has previously been used to probe error incorporation by eukaryotic RNA polymerase II (RNAPII) (Thomas et al., 1998) and *Escherichia coli* (*E. coli*) RNAP (Shaevitz et al., 2003). As P2 is neither structurally nor evolutionary related to the multisubunits RNAPs of cellular organisms (Mönttinen et al., 2014; Steitz, 1999), we first analyzed how P2 RdRP incorporates ITP in bulk experiments. We used ethidium bromide (EtBr) staining (Figure 3A, upper panel) and radiolabeling ([α-^{32}P]ITP) (Figure 3A, lower panel) to quantify the product synthesis and the ITP incorporation when one of the canonical NTPs was replaced with ITP. We observed that ITP could replace GTP, as the reaction successfully continues to completion (Figure 3A, lane "no GTP") with only a slight reduction in efficiency (Figure 3A, upper panel, compare lanes "no GTP" and "all NTPs"): this implies that ITP will frequently replace GTP in competitive nucleotide addition on a template cytosine. The intermediate band observed in the "no GTP" lane is likely due to secondary structures in the ssRNA template, which transiently stall P2 during the replication process. When replacing other nucleotides with ITP, no replication products were observed (Figure 3A): this implies that ITP acts as a mismatched base when pairing with G, U, and A in the template strand. The behavior of P2 in the presence of ITP is directly comparable to the behavior of RNAPII under similar conditions (Thomas et al., 1998), which implies that ITP can also be used to probe error incorporation by P2.

We next studied P2 transcription in the presence of ITP in our single-molecule assay. At 1-mM ITP, we observed a marked increase in the time spent in short pauses (Figure 3B), strongly suggesting that these pauses are connected to error incorporation. The empirical dwell-time distribution is well described by our stochastic-pausing model in the presence of ITP (Figures 3C and 3D).

Manganese Increases the Nucleotide Addition Rate and Lowers the Probability of P2 Pausing

Multiple studies on both DNA polymerases and RdRPs have shown that their fidelity is decreased when there is only manganese (i.e., no magnesium) present in the reaction buffer (Arnold et al., 2004; Beckman et al., 1985; Goodman et al., 1983). To investigate the effect of manganese on P2 elongation dynamics, we titrated the manganese concentration between 0 to 2 mM once the P2 has entered elongation (Supplemental Information). Varying the manganese concentration resulted in significant changes in the dwell-time distributions (Figure 4A): as the manganese concentration is increased, Pause 1 and Pause 2 probabilities decrease by 30%–40% and 60%–70%, respectively, and the Pause 1 exit rate increases by 30%–40%, while the Pause 2 exit rate shows no significant change. Additionally, the nucleotide addition rate increases by 10%–20% (Figures 4B and 4C). Taken together, these results are consistent with an increase in overall elongation rate with increased manganese concentrations, as reported in an earlier biochemical bulk study (Wright et al., 2012).

The Force Dependence of P2 Catalyzed RNA Elongation

P2 performs both replication and transcription on ssRNA templates. Here we observe the force dependence of P2 enzymatic activity when P2 has to displace the complementary strand of the template. In the applied force range (16–35 pN), the base pairs at the ds-ssRNA junction (Figure 1B) are destabilized by $0.6-2k_BT$ due to the applied force. We acquired approximately 45 traces per applied force at $[NTP]_{opt}$ (Figures 5A and S2B) and found that an increase in the force leaves the nucleotide-addition peak unaffected, but decreases the amount of time spent pausing (Figure 5A). The increased time spent pausing is quantitatively confirmed by the rate and probability estimates produced from fitting the dwell-time distributions (Figures 5B and 5C). In Figure S3D, we show how these results contrast

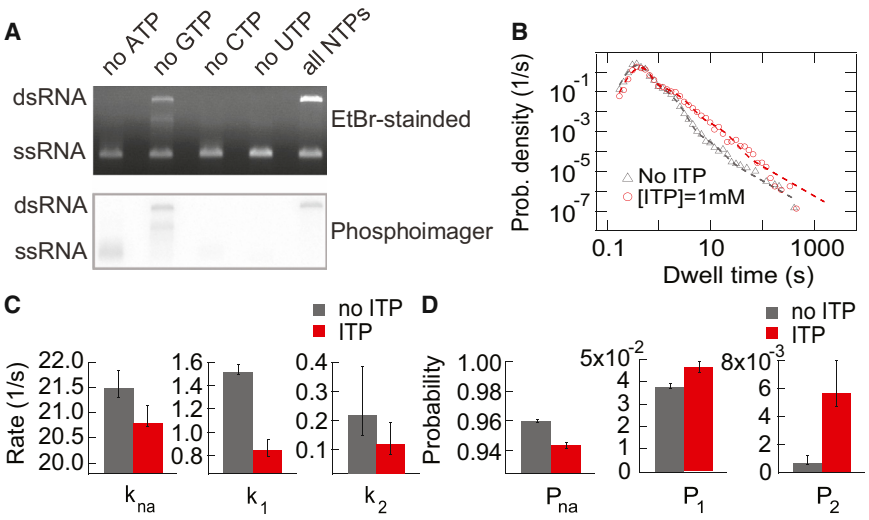

Figure 3. ITP Incorporation by P2 Slows Catalytic Activity and Increases Pause 2 Probability

(A) Replacement of GTP by ITP in P2-catalyzed replication reaction. Initiation reactions were carried out in the presence of 1-mM GTP and ATP. The formed elongation complexes were purified, and the formation of new initiation complexes was prevented by heparin. The subsequent elongation reactions were performed in $[NTP]_{opt,}$ supplemented with 35-nM [α-^{32}P]ITP (lane all NTPs) or in conditions where one of the canonical rNTPs was replaced with 1-mM ITP as indicated. The reaction products were analyzed by standard agarose gel electrophoresis using EtBr staining (upper) or visualization by phosphorimaging (lower). The mobility of the 2,948-nt-long ssRNA template and the dsRNA product is indicated on the left. The radioactively labeled ssRNA bands observed in the no-ATP and no-CTP lanes (lower) likely correspond elongation complexes that were stalled at early stage of the elongation phase, close to the 3′ end of the ssRNA template.

(B) Empirical dwell-time distribution from single molecule experiments with (red circles) and without (gray circles) ITP, at 30 pN force and $[NTP]_{opt}$. The dashed lines represent the MLE fits.

(C) Rates extracted from the MLE fits of the distributions in (B).

(D) Probabilities extracted from the MLE fits of the distributions in (B). The errors bars in (C) and (D) represent the standard deviation of a MLE procedure applied to 200 bootstrapped data sets.

with those that result from the use of the more standard approach of attempting to extract pause-free velocities from velocity histograms.

DISCUSSION

Basis for a Kinetic Model of P2-Catalyzed RNA Elongation

Our multiplexed magnetic-tweezers setup enables us to collect very large dwell-time data sets detailing the dynamics of the Φ6 RdRP P2 over four orders of magnitude in time. The size of the data sets allows us to appreciably constrain the type of models consistent with our data. We use MLE to analyze our dwell-time distributions. Similar stochastic analysis has previously been used in the study of ion channels (Colquhoun and Hawkes, 1995) and single-molecule fluorescence microscopy (Xie, 2001), but not in single-molecule force spectroscopy experiments—in part due to the relative paucity of data that could be collected. Using the Bayesian information criterion (Supplemental Information), we determine that the inclusion of at least two exponentially distributed short pauses is supported by the data. In constructing a kinetic model (Greive and von Hippel, 2005) of P2-catalyzed RNA elongation, we therefore choose to include the two simplest and most widely accepted pathways for polymerase pausing: pausing due to nucleotide misalignment arising from error incorporations (Johnson, 2008) (Figure S6A) and pausing that originates in a thermally driven large-scale conformational change that renders the enzyme catalytically inactive (Neuman et al., 2003) (Figure S6C).

Evidence for Two Distinct Nucleotide Addition Pathways

A key observation is that the pauses we identify fail to satisfy the nucleotide concentration dependencies expected for the two above-mentioned categories of off- and on-pathway pauses (for the full argument, see Supplemental Information, especially Figures S6A–S6D). In order to capture the observed decrease in pause lifetimes with increased nucleotide concentration (Figure 2B), we need to relax the assumption of complete catalytic inactivity (Donehower et al., 1977; Neuman et al., 2003) in the RdRP conformation responsible for the standard off-pathway pause (Figure 6A). To capture the concomitant decrease in pause probability, we further need to assume that nucleotide addition from the off-pathway configuration forces its reversal, bringing the RdRP back to its original on-pathway configuration (Figure 6A). With this, we can rationalize the concentration dependencies of Figure 2B in terms of Michaelis-Menten kinetics of nucleotide addition from different catalytically active configurations of the RdRP, with and without a mismatched terminal base (see Figure 6B and the discussion in next subsection). Interestingly, a recent fluorescence resonance energy transfer study (Brenlla et al., 2014) of an error-prone family Y DNA polymerase, related to RdRPs and RTs (Mönttinen et al., 2014), also provides evidence of an alternative pathway to increased error incorporation.

Long Pauses Directly Report on Single-Error Incorporation Events

We now expect one of our two observed pauses to correspond to a slowdown after an error has been incorporated; the probability of this pause should be a direct readout of the error rate of the process. Assuming Pause 1 is the pause reporting on errors unrealistically leads to an error estimate of one error every 26 ± 1 bp at $[NTP]_{opt}$ (Figure 2C), while assuming it is Pause 2 leads to an error estimate of one error every 1,350 ± 410 (Figure 2C), in broad agreement with error-estimates for related enzymes (Vignuzzi et al., 2006). This suggests that Pause 1

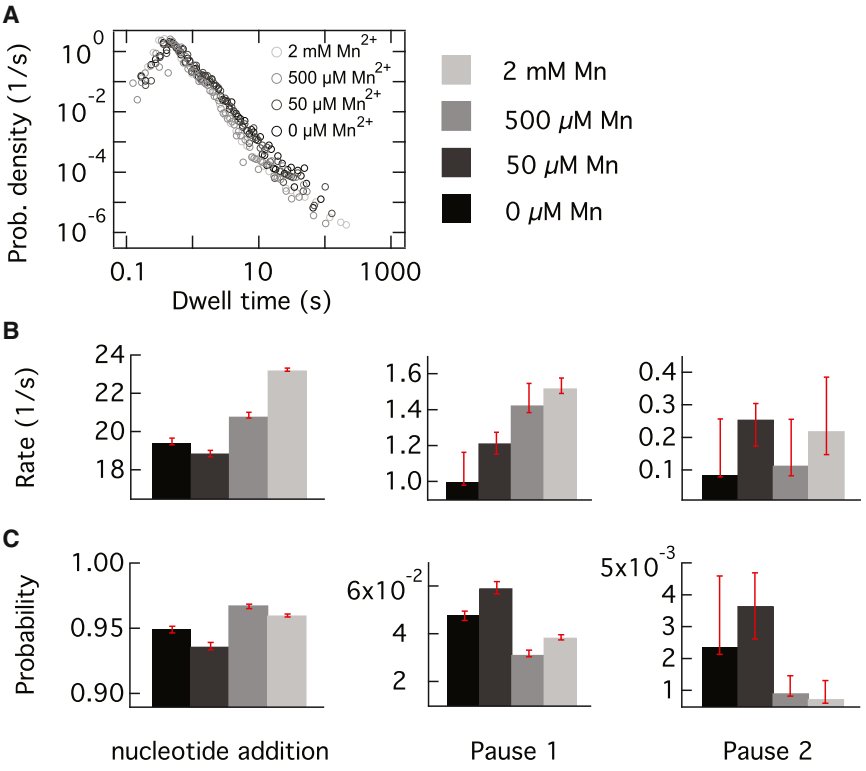

Figure 4. Mn^{2+} Increases the Nucleotide Addition Rate and Reduces the Probability of Pausing

(A) The empirical dwell-time distribution for four different concentrations of Mn^{2+}: 0 μM, 50 μM, 500 μM, and 2 mM. The concentration of Mg^{2+} is maintained constant at 5 mM, as is the nucleotide concentration (fixed at $[NTP]_{opt}$).

(B) The nucleotide addition rate, the Pause 1 exit rate, and the Pause 2 exit rate, plotted for the different manganese concentrations.

(C) The probabilities for P2 to be present in nucleotide addition, Pause 1, or Pause 2, plotted for the different manganese concentrations.

corresponds to the entrance into a long-lived elongation-competent state (Figure 2B), with a reduced—albeit nonzero—catalytic activity; Pause 2 arises from a catalytic slowdown (Figure 2B) when an error has just been incorporated, as is reported for other polymerases upon error incorporation (Johnson, 2008; Yang et al., 2012). Since the probability of entering Pause 2 is largely proportional to the probability of entering Pause 1 (Figure 2C), we infer that most errors are incorporated through the slow catalytic state that accompanies Pause 1, rendering this a fidelity-controlling pause. From here on we refer to the fast active state as the high-fidelity catalytic (HFC) state, the state corresponding to Pause 1 as the low-fidelity catalytic (LFC) state, and the state corresponding to Pause 2 as the terminal-base mismatched catalytic (TMC) state (Figure 6A). By considering Figures 2B and 6A, we can infer which path dominates the exit out of each state. Correct nucleotide addition dominates the exit from the HFC state, as most catalytic steps occur without pausing (P_{na} is close to one). The same holds true for LFC state, as the total exit rate from the LFC state depends on NTP concentration, and only a small fraction of transitions originating in the LFC state enters into the TMC state. The fact that the nucleotide addition rate in the TMC state is proportional to but lower than that of the LFC state (Figure 2B) indicates that the two states have a similar nucleotide dissociation constants, but that there is an increased barrier to nucleotide addition in the TMC.

Nucleotide Analog and Manganese Titration Confirm the Link between Long Pauses and Error Incorporation

To confirm that the long pauses observed are a direct result of error incorporation, we examined the effect of introducing ITP into the reaction buffer (Figures 3B–3D). Inosine has previously been shown to act like an error after incorporation by other polymerases (Martin et al., 1985; Matsuzaki et al., 1994), but to bind more strongly than a standard mismatch to the template base in the active site. Consequently, assays utilizing inosine will allow us to detect the effects of increased error incorporation already at modest levels of inosine. As the effect of ITP has not been established for P2, we first performed bulk experiments showing that ITP influences P2-directed RNA elongation in a manner consistent with the effect in other polymerases: it acts like an error when incorporated instead of all canonical bases apart from G, which it replaces with only a slight reduction in efficiency (Figure 3A). With the introduction of ITP in our buffer, we expect to see a rise in the probability of entering the TMC state. We also expect a modest reduction of nucleotide addition rate because ITP replaces GTP with a slight reduction in efficiency. As the entrance into the LFC state is assumed to be through a thermally driven transition in competition with nucleotide addition, we also expect a small rise in the probability of Pause 1 as the nucleotide addition rate is moderately decreased. The exit rate out of the LFC state (Pause 1) is also expected to decrease, as correct nucleotide addition is the dominant escape route and ITP is incorporated instead of GTP with a reduced efficiency. All of these effects are observed experimentally (Figures 3C and 3D). Additionally, and in accord with a run-off replication assay (Wright et al., 2012), our manganese titration experiments show that the nucleotide addition rate increases with manganese concentration (Figure 4B). With an increased nucleotide addition rate, we would expect a decreased entry to the LFC state and consequently a fall of the probabilities of both Pause 1 and Pause 2; this is also observed in our data (Figure 4C), adding further support to our model.

Interestingly, our manganese experiments lead to a different conclusion for polymerase fidelity from what has been proposed based on stop-flow experiment on the poliovirus RdRP. Replacing magnesium with manganese in the reaction buffer has previously been suggested to decrease RdRP fidelity (Arnold et al., 2004) not increase it, as suggested by our data (Figure 4C).

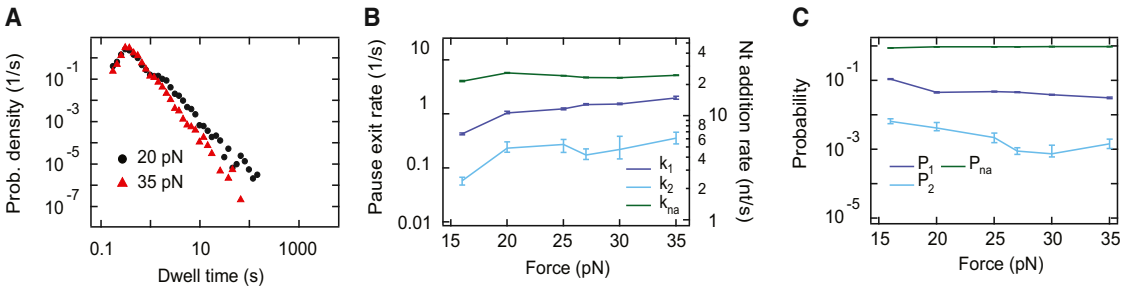

Figure 5. The Force Dependence of P2 Transcription

(A) The dwell-time distribution for two different applied forces at $[NTP]_{opt}$: black dots, 20 pN; red triangles, 35 pN.

(B) The pause exit and nucleotide addition rates as a function of force at $[NTP]_{opt}$. The error bars represent the SD of a MLE procedure applied to 200 bootstrapped data sets. The nucleotide addition rate (right axis) is represented by green dots connected by green lines as guides for the eye. The pause exit rates (left axis) are represented by dots connected by lines as guides for the eye (dark blue, k_1; cyan, k_2).

(C) Probability for P2 to be in one of the three different states (green, nucleotide addition; dark blue, Pause 1; cyan, Pause 2).

Possible explanations are that there is a significant enzymatic differences between the polio and the Φ6 RdRPs or that we did not completely replace magnesium with manganese in the reaction buffer. An interesting alternative explanation for the observed differences is that for enzymes with dual incorporation pathways, stop/quench flow assays are liable to skew the balance between the pathways used by allowing the HFC and LFC states to equilibrate between nucleotide additions. For our system, starving the polymerase of nucleotides would lead to an overestimate of error incorporation, an effect that is enhanced by the addition of manganese (Figure 4B), as it increases the catalytic rates.

Force Dependence of Pause Probabilities Suggests Translocation before Chemistry in the Slow Catalytic States

We observe no force dependence in the nucleotide addition rate from the HFC state, implying that either the translocation step is not rate limiting or that P2 translocates through a power stroke that renders it insensitive to the forces we apply. However, the nucleotide addition rates in the LFC and TMC states are still sensitive to force (Figure 5B). Fitting an Arrhenius law to the exit rates (Figure S4), we determine that the transition states are situated 0.17 ± 0.02 and 0.12 ± 0.09 nm from the pretranslocated position, respectively; these distances are consistent with the decrease in tether length due to the opening of one base pair in the tethered dsRNA (Figure S1C) and strongly suggest that the chemistry of bond formation does not provoke translocation in the LFC and TMC states, but rather that translocation of P2 is here thermally driven.

Conclusions

Here, we have extensively probed the mechanochemistry of viral mutagenesis. Specifically, we studied the elongation dynamics of P2 from bacteriophage Φ6, an established model system for RdRPs and RTs, by employing high-throughput magnetic tweezers combined with maximum-likelihood analysis. This approach has allowed us to capture the P2-catalyzed RNA elongation process for both correct and incorrect nucleotides with unprecedented detail. By analyzing how the replication dynamics of P2 RdRP are affected by nucleotide concentrations, destabilization of the fork, and the presence of both nucleotide analog and manganese, we have found strong evidence for a stochastic partitioning between two catalytically active configurations with different catalysis rates and substrate selectivity. Importantly, bulk techniques such as stop/quench flow assays would not be able to discriminate between the two catalytic pathways we have described and would always under estimate the fidelity of the polymerase.

Our observations are of both potential therapeutic and fundamental importance: identifying compounds that affect the probability of entering the fidelity controlling pause we describe here (Pause 1 in the above) might lead to ways of modifying mutation rates in RNA viruses and consequently decrease their pathogenicity; the gradual tuning of probabilities of entering fidelity controlling pauses might similarly be a general evolutionary strategy that allows viral populations to continuously adapt to the evolution of the hosts antiviral defenses. Such an evolutionary strategy is especially appealing since mutations at the active site of viral polymerases induce large fidelity changes (Vignuzzi et al., 2006) that may inactivate the virus (Acevedo et al., 2014). Using our novel approach for single-molecule error quantification at physiological nucleotide stoichiometry, future studies will examine whether the conclusions we draw for P2 hold true also for other polymerases.

Finally, and importantly, our high-throughput single-molecule approach is able to detail the dynamic behavior of enzymes over four orders of magnitude in time; used together with the accompanying theoretical modeling, this should help to usher in a mode of single-molecule approaches where a vast array of kinetic effects can be separated with statistical significance, increasing the biological impact of single-molecule studies. This is especially exciting in the context of understanding the molecular effect of drugs, as our approach has the potential to yield precise dynamic fingerprints of any antiviral drug (Crotty et al., 2000, 2001) affecting the elongation process.

EXPERIMENTAL PROCEDURES

Single-Molecule Transcription Experiments

Once the RNA construct length is calibrated inside a flow cell containing P2 reaction buffer (50-mM HEPES [pH 7.9], 20-mM ammonium acetate, 3% w/v polyethylene glycol 4,000 Da, 0.1-mM EDTA [pH 8.0], 5-mM $MgCl_2$, 2-mM $MnCl_2$, 0.01% Triton X-100, 5% Superase RNase inhibitor [Life Technologies],

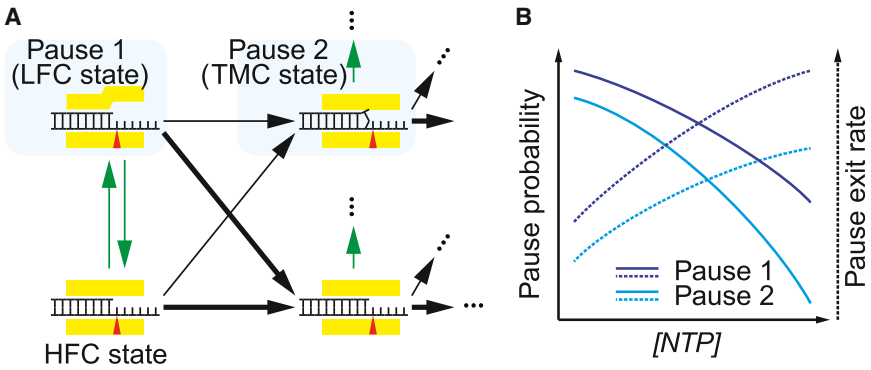

Figure 6. Model for On-Pathway Polymerase Pauses

(A) In our model, the polymerase has two catalytically active configurations, indicated by a narrow or wide space around the active site in the schematic polymerase structure (yellow). This, together with the state of the nascent RNA—having a terminal mismatch or not—gives rise to our two observed pause types. The resulting states for the RdRP and RNA are an HFC state, which is fast, without terminal mismatch, and with a low error rate; a LFC state, which is slow, without terminal mismatch, error prone, and entered through a thermal transition from the HFC state; and a TMC state, entered upon error incorporation, where nucleotide misalignment results in very slow nucleotide addition (Pause 2). In the reaction scheme, black arrows represent transitions dependent on nucleotide concentration, while green arrows represent thermal transitions. The thick arrow out of each state represents the dominant path to leave that state, as deduced from our experimental observations (see main text).

(B) The expected trends in pause probabilities and pause exit rates as a function of NTP concentration for the pauses in (A). These rates are dominated by the transitions indicated by thick arrows in (A), and from Figure 2B, we see that these exit rates are consistent with Michaelis-Menten kinetics.

and 20-μg/ml BSA) (see Supplemental Information for P2 and RNA production and Figure S1A for the RNA construct), 9 nM of P2 is flushed in. We perform experiments at 21°C for 1 hr at constant force and fixed NTP concentration while recording images of the magnetic beads at 25 Hz. Because of the large field of view of our camera we are able to follow up to 200 tethers at a time (Cnossen et al., 2014; De Vlaminck et al., 2011). The recorded images of the beads are converted into (*x*, *y*, *z*) positions using custom-written routines in Labview (Lipfert et al., 2011; van Loenhout et al., 2012). Distinct traces are low-pass filtered at 0.5 Hz, providing an optical resolution of 0.3 nm along the optical axis (*z* axis) (Figure S2B) and synchronized with regards to starting position. The changes in extension are converted into the numbers of transcribed nucleotides using the force-extension relationships for dsRNA and ssRNA constructs obtained in P2 reaction buffer (Figure 2B) (Maier et al., 2000).

Stalling Reaction with P2

Following a 30-min incubation with the P2 initiation buffer (P2 reaction buffer supplemented with 1-mM rATP, 1-mM rGTP, 0.2-mM rCTP), we rinse the reaction chamber with an excess amount of P2 reaction buffer containing 0.5% Superase RNase inhibitor (Life Technologies) (no NTPs). We then trigger elongation by adding P2 reaction buffer supplemented with rNTPs (and ITP) as indicated. The dynamic of P2 is not affected by the stalling reaction (Figure S5). In the case of the Mn^{2+} titration experiments, no EDTA was added into the P2 reaction buffer for all experiments containing less than 2-mM Mn^{2+}.

Bulk Replication Experiments

RNA replication reactions were carried out in 50-mM HEPES (pH 7.5), 20-mM ammonium acetate, 6% (w/v) polyethylene glycol 4000, 5-mM $MgCl_2$, 2-mM $MnCl_2$, 0.1-mM EDTA, 0.1% Triton X-100, and 0.8-U/μl RNasin Ribo Lock (Thermo Scientific). Initiation reactions were carried out (125-nM ssRNA and 500-nM P2) in the presence of 1-mM rGTP and rATP (to allow the synthesis of the first 10 nts complementary to the 3′ end of the ssRNA template) at +30°C for 20 min, the formed elongation complexes were purified using Sephacryl S-300 matrix (Pharmacia) and the reaction buffer with no NTPs for elution. The formation of new initiation complexes was prevented by heparin (5 mg/ml), and the incubation was continued at +30°C for 5 min. The subsequent elongation reactions were supplemented with 0.2 mCi/ml of [α-^{32}P]ITP (6,000 Ci/mmol; Cambro Scientific GmbH) and the indicated nucleotides, and the incubation at +30°C was continued for 2 hr.

Generation of Empirical Dwell-Time Distributions

When constructing empirical dwell-time distributions, dwell-times from different polymerases operating at identical conditions were grouped together (Figure S1E). Looking at dwell-time distribution for individual polymerases, a small percentage consistently spend a much longer than average time pausing; to prevent these pause-prone polymerases from biasing the data, we remove the 5% with the highest and lowest dwell-time densities at 3 s.

SUPPLEMENTAL INFORMATION

Supplemental Information includes Supplemental Experimental Procedures and six figures and can be found with this article online at http://dx.doi.org/10.1016/j.celrep.2015.01.031.

AUTHOR CONTRIBUTIONS

D.D., I.D.V., and N.H.D. designed the research and the single-molecule experiments. D.D. designed and assembled the magnetic tweezers apparatus. D.D., I.D.V., and B.A.B. undertook the experiments. I.D.V. and S.H. designed and D.D., I.D.V., and S.H. made the RNA construct. M.M.P. and D.H.B. provided the purified Φ6 RdRP. M.M.P. performed the radioactive ITP assay. M.D. developed the application of MLE to the force spectroscopy data. D.D. and M.D. analyzed and interpreted the data. D.D., M.D., and N.H.D. wrote the paper.

ACKNOWLEDGMENTS

We thank Wiecher Kamping and Quinten Esajas for preliminary contributions to this work; Riitta Tarkiainen for technical assistance; Iwijn de Vlaminck for help with the experimental configuration; Jelmer Cnossen for assistance with software; Eric Sniider, Clara Posthuma, Jan Lipfert, and Craig Cameron for fruitful discussions; and Christophe Danelon, Clara Posthuma, and Jan Lipfert for critically reading the manuscript. This work was financially supported by the Academy of Finland grants 272507, 250113, and 256069 to M.M.P., grants 255342 and 256518 to D.H.B., and grants from the Sigrid Jusélius Foundation to D.H.B. and M.M.P. jointly, as well as by a TU Delft startup grant to M.D. and by a EURYI grant from the European Science Foundation and a TOP grant from the Netherlands Organisation for Scientific Research to N.H.D.

Received: August 29, 2014
Revised: December 23, 2014
Accepted: January 10, 2015
Published: February 12, 2015

REFERENCES

Acevedo, A., Brodsky, L., and Andino, R. (2014). Mutational and fitness landscapes of an RNA virus revealed through population sequencing. Nature *505*, 686–690.

Arnold, J.J., Gohara, D.W., and Cameron, C.E. (2004). Poliovirus RNA-dependent RNA polymerase (3Dpol): pre-steady-state kinetic analysis of ribonucleotide incorporation in the presence of Mn^{2+}. Biochemistry *43*, 5138–5148.

Beckman, R.A., Mildvan, A.S., and Loeb, L.A. (1985). On the fidelity of DNA replication: manganese mutagenesis in vitro. Biochemistry *24*, 5810–5817.

Brenlla, A., Markiewicz, R.P., Rueda, D., and Romano, L.J. (2014). Nucleotide selection by the Y-family DNA polymerase Dpo4 involves template translocation and misalignment. Nucleic Acids Res. *42*, 2555–2563.

Butcher, S.J., Grimes, J.M., Makeyev, E.V., Bamford, D.H., and Stuart, D.I. (2001). A mechanism for initiating RNA-dependent RNA polymerization. Nature *410*, 235–240.

Cheung, A.C., and Cramer, P. (2011). Structural basis of RNA polymerase II backtracking, arrest and reactivation. Nature *471*, 249–253.

Cnossen, J.P., Dulin, D., and Dekker, N.H. (2014). An optimized software framework for real-time, high-throughput tracking of spherical beads. Rev. Sci. Instrum. *85*, 103712.

Colquhoun, D., and Hawkes, A.G. (1995). The principles of the Stochastic Interpretation of Ion-Channel Mechanism. In Single-Channel Recording, Second Edition, B. Sakmann and E. Neher, eds. (New York: Plenum Press), pp. 397–481.

Crotty, S., Maag, D., Arnold, J.J., Zhong, W., Lau, J.Y., Hong, Z., Andino, R., and Cameron, C.E. (2000). The broad-spectrum antiviral ribonucleoside ribavirin is an RNA virus mutagen. Nat. Med. *6*, 1375–1379.

Crotty, S., Cameron, C.E., and Andino, R. (2001). RNA virus error catastrophe: direct molecular test by using ribavirin. Proc. Natl. Acad. Sci. USA *98*, 6895–6900.

De Vlaminck, I., Henighan, T., van Loenhout, M.T., Pfeiffer, I., Huijts, J., Kerssemakers, J.W., Katan, A.J., van Langen-Suurling, A., van der Drift, E., Wyman, C., and Dekker, C. (2011). Highly parallel magnetic tweezers by targeted DNA tethering. Nano Lett. *11*, 5489–5493.

Depken, M., Galburt, E.A., and Grill, S.W. (2009). The origin of short transcriptional pauses. Biophys. J. *96*, 2189–2193.

Donehower, L., Wong-Staal, F., and Gillespie, D. (1977). Divergence of baboon endogenous type C virogenes in primates: genomic viral RNA in molecular hybridization experiments. J. Virol. *21*, 932–941.

Dulin, D., Lipfert, J., Moolman, M.C., and Dekker, N.H. (2013). Studying genomic processes at the single-molecule level: introducing the tools and applications. Nat. Rev. Genet. *14*, 9–22.

Galburt, E.A., Grill, S.W., Wiedmann, A., Lubkowska, L., Choy, J., Nogales, E., Kashlev, M., and Bustamante, C. (2007). Backtracking determines the force sensitivity of RNAP II in a factor-dependent manner. Nature *446*, 820–823.

Geertsema, H.J., and van Oijen, A.M. (2013). A single-molecule view of DNA replication: the dynamic nature of multi-protein complexes revealed. Curr. Opin. Struct. Biol. *23*, 788–793.

Goodman, M.F., Keener, S., Guidotti, S., and Branscomb, E.W. (1983). On the enzymatic basis for mutagenesis by manganese. J. Biol. Chem. *258*, 3469–3475.

Greive, S.J., and von Hippel, P.H. (2005). Thinking quantitatively about transcriptional regulation. Nat. Rev. Mol. Cell Biol. *6*, 221–232.

Jin, Z., Deval, J., Johnson, K.A., and Swinney, D.C. (2011). Characterization of the elongation complex of dengue virus RNA polymerase: assembly, kinetics of nucleotide incorporation, and fidelity. J. Biol. Chem. *286*, 2067–2077.

Jin, Z., Leveque, V., Ma, H., Johnson, K.A., and Klumpp, K. (2012). Assembly, purification, and pre-steady-state kinetic analysis of active RNA-dependent RNA polymerase elongation complex. J. Biol. Chem. *287*, 10674–10683.

Johnson, K.A. (2008). Role of induced fit in enzyme specificity: a molecular forward/reverse switch. J. Biol. Chem. *283*, 26297–26301.

Larson, M.H., Landick, R., and Block, S.M. (2011). Single-molecule studies of RNA polymerase: one singular sensation, every little step it takes. Mol. Cell *41*, 249–262.

Lauring, A.S., Frydman, J., and Andino, R. (2013). The role of mutational robustness in RNA virus evolution. Nat. Rev. Microbiol. *11*, 327–336.

Lipfert, J., Kerssemakers, J.J., Rojer, M., and Dekker, N.H. (2011). A method to track rotational motion for use in single-molecule biophysics. Rev. Sci. Instrum. *82*, 103707.

Maier, B., Bensimon, D., and Croquette, V. (2000). Replication by a single DNA polymerase of a stretched single-stranded DNA. Proc. Natl. Acad. Sci. USA *97*, 12002–12007.

Makeyev, E.V., and Bamford, D.H. (2000a). The polymerase subunit of a dsRNA virus plays a central role in the regulation of viral RNA metabolism. EMBO J. *19*, 6275–6284.

Makeyev, E.V., and Bamford, D.H. (2000b). Replicase activity of purified recombinant protein P2 of double-stranded RNA bacteriophage phi6. EMBO J. *19*, 124–133.

Makeyev, E.V., and Grimes, J.M. (2004). RNA-dependent RNA polymerases of dsRNA bacteriophages. Virus Res. *101*, 45–55.

Martin, F.H., Castro, M.M., Aboul-ela, F., and Tinoco, I., Jr. (1985). Base pairing involving deoxyinosine: implications for probe design. Nucleic Acids Res. *13*, 8927–8938.

Matsuzaki, H., Kassavetis, G.A., and Geiduschek, E.P. (1994). Analysis of RNA chain elongation and termination by Saccharomyces cerevisiae RNA polymerase III. J. Mol. Biol. *235*, 1173–1192.

Mönttinen, H.A., Ravantti, J.J., Stuart, D.I., and Poranen, M.M. (2014). Automated structural comparisons clarify the phylogeny of the right-hand-shaped polymerases. Mol. Biol. Evol. *31*, 2741–2752.

Neuman, K.C., Abbondanzieri, E.A., Landick, R., Gelles, J., and Block, S.M. (2003). Ubiquitous transcriptional pausing is independent of RNA polymerase backtracking. Cell *115*, 437–447.

Ng, K.K., Arnold, J.J., and Cameron, C.E. (2008). Structure-function relationships among RNA-dependent RNA polymerases. Curr. Top. Microbiol. Immunol. *320*, 137–156.

Salgado, P.S., Makeyev, E.V., Butcher, S.J., Bamford, D.H., Stuart, D.I., and Grimes, J.M. (2004). The structural basis for RNA specificity and Ca^{2+} inhibition of an RNA-dependent RNA polymerase. Structure *12*, 307–316.

Sarin, L.P., Poranen, M.M., Lehti, N.M., Ravantti, J.J., Koivunen, M.R., Aalto, A.P., van Dijk, A.A., Stuart, D.I., Grimes, J.M., and Bamford, D.H. (2009). Insights into the pre-initiation events of bacteriophage phi 6 RNA-dependent RNA polymerase: towards the assembly of a productive binary complex. Nucleic Acids Res. *37*, 1182–1192.

Schwarz, G. (1978). Estimating dimension of a model. Ann. Stat. *6*, 461–464.

Shaevitz, J.W., Abbondanzieri, E.A., Landick, R., and Block, S.M. (2003). Backtracking by single RNA polymerase molecules observed at near-base-pair resolution. Nature *426*, 684–687.

Steitz, T.A. (1999). DNA polymerases: structural diversity and common mechanisms. J. Biol. Chem. *274*, 17395–17398.

Thomas, M.J., Platas, A.A., and Hawley, D.K. (1998). Transcriptional fidelity and proofreading by RNA polymerase II. Cell *93*, 627–637.

van Loenhout, M.T., Kerssemakers, J.W., De Vlaminck, I., and Dekker, C. (2012). Non-bias-limited tracking of spherical particles, enabling nanometer resolution at low magnification. Biophys. J. *102*, 2362–2371.

Vignuzzi, M., Stone, J.K., and Andino, R. (2005). Ribavirin and lethal mutagenesis of poliovirus: molecular mechanisms, resistance and biological implications. Virus Res. *107*, 173–181.

Vignuzzi, M., Stone, J.K., Arnold, J.J., Cameron, C.E., and Andino, R. (2006). Quasispecies diversity determines pathogenesis through cooperative interactions in a viral population. Nature *439*, 344–348.

Vignuzzi, M., Wendt, E., and Andino, R. (2008). Engineering attenuated virus vaccines by controlling replication fidelity. Nat. Med. *14*, 154–161.

Vilfan, I.D., Candelli, A., Hage, S., Aalto, A.P., Poranen, M.M., Bamford, D.H., and Dekker, N.H. (2008). Reinitiated viral RNA-dependent RNA polymerase resumes replication at a reduced rate. Nucleic Acids Res. *36*, 7059–7067.

Voliotis, M., Cohen, N., Molina-París, C., and Liverpool, T.B. (2008). Fluctuations, pauses, and backtracking in DNA transcription. Biophys. J. *94*, 334–348.

Wright, S., Poranen, M.M., Bamford, D.H., Stuart, D.I., and Grimes, J.M. (2012). Noncatalytic ions direct the RNA-dependent RNA polymerase of bacterial double-stranded RNA virus ϕ6 from de novo initiation to elongation. J. Virol. *86*, 2837–2849.

Xie, S.N. (2001). Single-molecule approach to enzymology. Single Mol. *2*, 229–236.

Yang, X., Smidansky, E.D., Maksimchuk, K.R., Lum, D., Welch, J.L., Arnold, J.J., Cameron, C.E., and Boehr, D.D. (2012). Motif D of viral RNA-dependent RNA polymerases determines efficiency and fidelity of nucleotide addition. Structure *20*, 1519–1527.